840 *Chem. Mater.* **2010,** *22,* 840–850
DOI:10.1021/cm901633r

CHEMISTRY OF MATERIALS
Article

New Manganese-Bearing Antimonides and Bismuthides with Complex Structures. Synthesis, Structural Characterization, and Electronic Properties of $Yb_9Mn_{4+x}Pn_9$ (Pn = Sb or Bi)†

Sheng-Qing Xia‡,§ and Svilen Bobev*,‡

‡*Department of Chemistry and Biochemistry, University of Delaware, Newark, Delaware 19716, and* §*State Key Laboratory of Crystal Materials, Institute of Crystal Materials, Shandong University, Jinan, Shandong 250100, P.R.C.*

Received June 12, 2009. Revised Manuscript Received August 5, 2009

Reported are structure and property studies on a series of isostructural compounds with general formulas $Yb_9Mn_{4+x}Sb_9$ ($x \approx 0.2$), $A_9Mn_{4+x}Bi_9$ (A = Ca and Yb; $x \approx 0$), and the Zn-substituted derivatives $Yb_9(Mn,Zn)_{4+x}Sb_9$ ($0 < x < 0.4$). They have been synthesized from the corresponding elements by high-temperature reactions, and their structures have been established by single-crystal X-ray diffraction. Despite being nearly stoichiometric phases, whose average crystallographic arrangement can be described with the orthorhombic $Ca_9Mn_4Bi_9$ type structure (space group *Pbam*, No. 55), these ternary materials exist within narrow homogeneity ranges, whereupon an interstitial site is partially occupied by the transition metal. Electronic structure calculations confirm that the "empty" $A_9Mn_4Sb_9$ or $A_9Mn_4Bi_9$ structures are electron deficient, making them suitable hosts for small dopant atoms. The expected poorly metallic behavior is evidenced from temperature-dependent resistivity data gathered from single-crystals. Magnetic susceptibility measurements in the range 2−350 K reveal complex antiferromagnetically coupled structures. These experimental results are further corroborated by theoretical calculations based on the linear muffin-tin orbital (LMTO) and the full potential linearized augmented plane wave (FP-LAPW) methods.

Introduction

In recent years, there has been a renewed interest in transition metal Zintl phases[1] as promising materials for thermoelectric applications.[2−11] Such compounds contain electronegative p-block elements and d-metals, which are bound through strong directional (covalent) interactions to form polyanionic networks, whereas the cation−anion interactions are more electrostatic than covalent in character. Therefore, these materials are neither typical valence compounds nor typical intermetallics and exhibit poorly metallic or small band gap semiconducting electronic properties. Such multifaceted structural characteristics provide almost unlimited potential for alterations on the cation and anion sites and fine-tuning of the transport properties—an added benefit for the optimization of the thermoelectric figure of merit ZT.[11] A proof of principle of this concept is the complex Zintl phase $Yb_{14}MnSb_{14}$,[4] which can be brought up as an example of this "class of thermoelectric materials."[4]

The unique aspects of the chemistry and physics of the Zintl phases with d-metals have been at the focus of many previous studies,[12−23] including work from

†Accepted as part of the 2010 "Materials Chemistry of Energy Conversion Special Issue".

*Corresponding author. Phone: (302) 831-8720. Fax: (302) 831-6335. E-mail: bobev@udel.edu.

(1) Kauzlarich, S. M., Ed. *Chemistry, Structure and Bonding in Zintl Phases and Ions*; VCH: New York, 1996, and references therein.
(2) Snyder, G. J.; Toberer, E. S. *Nat. Mater.* **2008**, *7*, 105–114.
(3) Kauzlarich, S. M.; Brown, S. R.; Snyder, G. J. *Dalton Trans.* **2007**, *21*, 2099–2100.
(4) Brown, S. R.; Kauzlarich, S. M.; Gascoin, F.; Snyder, G. J. *Chem. Mater.* **2006**, *18*, 1873–1877.
(5) Toberer, E. S.; Cox, C. A.; Brown, S. R.; Ikeda, T.; May, A. F.; Kauzlarich, S. M.; Snyder, G. J. *Adv. Funct. Mater.* **2008**, *18*, 2795–2800.
(6) Brown, S. R.; Toberer, E. S.; Ikeda, T.; Cox, C. A.; Gascoin, F.; Kauzlarich, S. M.; Snyder, G. J. *Chem. Mater.* **2008**, *20*, 3412–3419.
(7) Wang, X. J.; Tang, M. B.; Chen, H. H.; Yang, X. X.; Zhao, J. T.; Burkhardt, U.; Grin, Y. *App. Phys. Lett.* **2009**, *94*, 092106.
(8) Gascoin, F.; Ottensmann, S.; Stark, D.; Haile, S. M.; Snyder, G. J. *Adv. Funct. Mater.* **2005**, *15*, 1860–1864.
(9) Wang, X. J.; Tang, M. B.; Zhao, J. T.; Chen, H. H.; Yang, X. X. *App. Phys. Lett.* **2007**, *90*, 232107.
(10) Todorov, I.; Chung, D. Y.; Ye, L.; Freeman, A. J.; Kanatzidis, M. G. *Inorg. Chem.* **2009**, *48*, 4768–4776.
(11) Madsen, G. K. H. *J. Am. Chem. Soc.* **2006**, *128*, 12140–12146.
(12) Chan, J. Y.; Kauzlarich, S. M.; Klavins, P.; Shelton, R. N.; Webb, D. J. *Chem. Mater.* **1997**, *9*, 3132–3135.
(13) Jiang, J.; Kauzlarich, S. M. *Chem. Mater.* **2006**, *18*, 435–441.
(14) Sánchez-Portal, D.; Martin, R. M.; Kauzlarich, S. M.; Pickett, W. E. *Phys. Rev. B* **2002**, *65*, 144414.
(15) Holm, A. P.; Kauzlarich, S. M.; Morton, S. A.; Waddill, G. D.; Pickett, W. E.; Tobin, J. G. *J. Am. Chem. Soc.* **2002**, *124*, 9894–9898.
(16) Fisher, I. R.; Bud'ko, S. L.; Song, C.; Canfield, P. C.; Ozawa, T. C.; Kauzlarich, S. M. *Phys. Rev. Lett.* **2000**, *85*, 1120.
(17) Holm, A. P.; Olmstead, M. M.; Kauzlarich, S. M. *Inorg. Chem.* **2003**, *42*, 1973–1981.
(18) Kim, H.; Condron, C. L.; Holm, A. P.; Kauzlarich, S. M. *J. Am. Chem. Soc.* **2000**, *122*, 10720–10721.
(19) Park, S. M.; Kim, S. J.; Kanatzidis, M. G. *Inorg. Chem.* **2005**, *44*, 4979–4982.
(20) Kuromoto, T. Y.; Kauzlarich, S. M.; Webb, D. J. *Chem. Mater.* **1992**, *4*, 435–440.
(21) Holm, A. P.; Park, S.-M.; Condron, C. L.; Kim, H.; Klavins, P.; Grandjean, F.; Hermann, R. P.; Long, G. J.; Kanatzidis, M. G.; Kauzlarich, S. M.; Kim, S.-J. *Inorg. Chem.* **2003**, *42*, 4660–4667.
(22) Ahmadpour, F.; Kolodiazhnyi, T.; Mozharivskyj, Y. *J. Solid State Chem.* **2007**, *180*, 2420–2428.

 Published on Web 08/26/2009

our laboratory.[24−32] From these, it becomes clear that the correlations between the crystal structures and the physical properties in such compounds are rather difficult to interpret. After all, the Zintl reasoning[1] has been developed with main-group elements in mind, and it is not always suitable for open-shell configurations, common for the d-metals. This point is illustrated by the following Mn-containing antimonides and bismuthides—$Ca_{21}Mn_4Sb_{18}$,[17] $Sr_{21}Mn_4Sb_{18}$,[18] Sr_2MnSb_2,[19] $Ca_{14}MnBi_{11}$,[20] $Eu_{10}Mn_6Sb_{13}$,[21] $CaMn_2Sb_2$ and $SrMn_2Sb_2$,[27] $Ca_{21}Mn_4Bi_{18}$,[28] and $BaMn_2Sb_2$[29]—all of which have distinctive magnetic and electronic, properties arising from the presence of Mn^{2+} ions (formally d^5) in special coordination environments. In certain cases, isomorphous substitutions of Mn^{2+} with Zn^{2+} (or Cd^{2+}, both formally d^{10}) are possible, allowing for simpler structure rationalization.[22,29] In some other instances, the same structures either cannot be realized, or if they can, there are subtle structural differences.[18,28,32] Other impediments can result from fluctuating valencies or from the presence of interstitials, a signature of the title compounds $A_9Mn_{4+x}Pn_9$ (A = Ca and Yb; Pn = Sb, Bi), and their Zn and Cd analogs $A_9Zn_{4+x}Pn_9$ and $A_9Cd_{4+x}Pn_9$ ($0 \le x \le 0.5$).[23−25,33]

Compounds with the nominal "9-4-9" formula can be dated back to the late 1970s, when $Ca_9Mn_4Bi_9$ was first synthesized.[33] For many years, the structure type named after this phase (Pearson's symbol $oP44$)[34] encompassed only a few other examples.[35] In 2001, the isostructural $Yb_9Zn_4Bi_9$ was reported and noted to be one-electron richer (and therefore electron precise) compared to its $Ca_9Zn_4Bi_9$ analog.[23] This, together with the 2004 report on the interstitially stabilized $Yb_9Zn_{4+x}Sb_9$ and $Ca_9Zn_{4+x}Sb_9$ ($x \approx 0.5$) called into question the originally proposed Zintl-like electron count and fully ordered structure.[24] Very recently, by a combination of accurate single-crystal refinements and electronic structure calculations,[25] these issues were settled for all Zn- and Cd-containing containing $A_9Zn_{4+x}Pn_9$ and $A_9Cd_{4+x}Pn_9$ (A = Ca, Sr, Yb, Eu; Pn = Sb, Bi; $0 \le x \le 0.5$) phases. With this paper, we report the synthesis, crystal structure, electronic structure, and properties of the new compounds $Yb_9Mn_{4+x}Sb_9$ ($x \approx 0.2$) and $Yb_9Mn_{4+x}Bi_9$ ($x \approx 0$; $Yb_9Mn_4Bi_9$ hereafter). The structures and the properties of the solid solutions $Yb_9(Mn,Zn)_{4+x}Sb_9$ ($0 < x < 0.4$) are also presented. In addition, theoretical calculations based on the density function method are discussed in the context of the electronic and magnetic properties of these compounds.

Experimental Section

Synthesis. The metals were purchased from Alfa or Ames Laboratory (>99.9%) and were used as received. To avoid oxidation of the raw materials, we performed all manipulations inside an argon-filled glovebox with controlled oxygen and moisture levels below 1 ppm or under a vacuum. Two different types of reactions were explored: (i) melting stoichiometric mixtures of the elements; (ii) flux-type reactions using various low-melting metals as a crystal growth medium. The former were carried out in welded Nb tubes, which were subsequently jacketed in fused silica ampules and flame-sealed under a vacuum. Mixtures containing the starting materials in stoichiometric ratios were heated to 1273 or 1373 K (300°/h), equilibrated for 24 h, and then cooled to room temperature (10°/h rate). The tubes were brought back in the glovebox and opened. The reaction products were usually polycrystalline, but under a microscope, very small crystals with dark-to-black appearance and with irregular morphology were visible; they were suitable for single-crystal X-ray diffraction work (vide infra).

In the typical flux-experiments, mixtures of the elements in a molar ratio A:Mn:Pn = 2:1:2 were loaded in 2 cm^3 alumina crucibles. The crucibles were then topped off with Pb metal (mp 601 K) in 20-fold excess, placed in 1/2 in. fused silica tubes and sealed under vacuum. The reactions were heated to 1273 K (300°/h), equilibrated at this temperature for 20 h, and subsequently cooled to 873 K (20°/h). Afterward, the molten flux was easily removed by decanting it, leaving behind small needle-shaped crystals in the crucibles. They were brittle and had distinctive appearance with dark-metallic luster. Small amounts of $A_{11}Pn_{10}$[34] (A = Ca, Yb; Pn = Sb, Bi; irregular crystals with silver luster) were a common side-product, and were mechanically separated from the rest of the sample.

This technique worked best for $Yb_9Mn_{4+x}Sb_9$, where some of the crystals were 5−6 mm long, but was not advantageous for the synthesis of the Bi analogs. Other metal fluxes were also tried using the same temperature profile, but were not found suitable. For example, the reaction described above ran with Ga or In as a flux produced crystals of the known $Yb_{11}GaSb_9$[31] and $Yb_{11}InSb_9$ phases;[30] use of Sn in place of Pb (under the same conditions) favored the growth of other known phases—$YbMn_2Sb_2$[36] and $Yb_{14}MnSb_{11}$.[4] Reactions with an excess of Bi as a self-flux were also tried, but yielded $A_{11}Bi_{10}$[34] (A = Ca, Yb). Employing Zn or Zn/Pb mixture as a flux afforded the synthesis of the solid solutions $Yb_9(Mn,Zn)_{4+x}Sb_9$ ($0 < x < 0.4$).

We also note that all attempts to extend this series were unsuccessful. Because both $Yb_9Mn_4Bi_9$ and $Ca_9Mn_4Bi_9$ exist, and since the ionic radii of Ca^{2+} and Yb^{2+} are almost the same,[37] it was logical to consider the synthesis of $Ca_9Mn_{4+x}Sb_9$—an alkaline-earth metal analog of $Yb_9Mn_{4+x}Sb_9$.

(23) Kim, S.-J.; Salvador, J.; Bilc, D.; Mahanti, S. D.; Kanatzidis, M. G. *J. Am. Chem. Soc.* **2001**, *123*, 12704–12705.
(24) Bobev, S.; Thompson, J. D.; Sarrao, J. L.; Olmstead, M. M.; Hope, H.; Kauzlarich, S. M. *Inorg. Chem.* **2004**, *43*, 5044–5052.
(25) Xia, S.-Q.; Bobev, S. *J. Am. Chem. Soc.* **2007**, *129*, 10011–10018.
(26) Xia, S.-Q.; Bobev, S. *J. Am. Chem. Soc.* **2007**, *129*, 4049–4057.
(27) Bobev, S.; Merz, J.; Lima, A.; Fritsch, V.; Thompson, J. D.; Sarrao, J. L.; Gillessen, M.; Dronskowski, R. *Inorg. Chem.* **2006**, *45*, 4047–4054.
(28) Xia, S.-Q.; Bobev, S. *Inorg. Chem.* **2007**, *46*, 874–883.
(29) Xia, S.-Q.; Myers, C.; Bobev, S. *Eur. J. Inorg. Chem.* **2008**, 4262–4269.
(30) Xia, S.-Q.; Hullmann, J.; Bobev, S.; Ozbay, A.; Nowak, E. R.; Fritsch, V. *J. Solid State Chem.* **2007**, *180*, 2088–2094.
(31) Bobev, S.; Fritsch, V.; Thompson, J. D.; Sarrao, J. L.; Eck, B.; Dronskowski, R.; Kauzlarich, S. M. *J. Solid State Chem.* **2005**, *178*, 1071–1079.
(32) Xia, S.-Q.; Bobev, S. *Inorg. Chem.* **2008**, *47*, 1919–1921.
(33) Brechtel, E.; Cordier, G.; Schäfer, H. *Z. Naturforsch.* **1979**, *34B*, 1229–1233.
(34) Villars, P.; Calvert, L. D. *Pearson's Handbook of Crystallographic Data for Intermetallic Phases*, 2nd ed.; American Society for Metals: Materials Park, OH, 1991.
(35) Brechtel, E.; Cordier, G.; Schäfer, H. *Z. Naturforsch.* **1981**, *36B*, 1099–1104.
(36) Morozkin, A. V.; Isnard, O.; Henry, P.; Granovsky, S.; Nirmala, R.; Manfrinetti, P. *J. Alloys Compd.* **2006**, *420*, 34–36.
(37) Shannon, R. D.; Prewitt, C. T. *Acta Crystallogr., Sect. B* **1969**, *25*, 925–945.

Table 1. Selected Single-Crystal Data Collection and Refinement Parameters for $A_9Mn_{4+x}Pn_9$ (A = Ca or Yb; Pn = Sb or Bi) and the Solid Solutions $Yb_9(Mn,Zn)_{4+x}Sb_9$ ($0 < x < 0.4$); For the Sake of Better Comparison, Refinement Parameters for $Yb_9Zn_{4+x}Sb_9$ Are Also Included

	$Yb_9Mn_{4.18(2)}Sb_9$	$Yb_9Zn_{4.18(2)}Sb_9$	$Yb_9Mn_{2.8}Zn_{1.6(1)}Sb_9$	$Yb_9Mn_{0.5}Zn_{3.9(1)}Sb_9$	$Yb_9Mn_4Bi_9$	$Ca_9Mn_4Bi_9$
fw, $Z = 2$	2882.76	2926.36	2911.79	2932.78	3657.94	2461.30
radiation type, wavelength	Mo Kα, 0.71073 Å					
temperature (K)	90(2)					
space group	*Pbam* (No. 55)					
a (Å)	22.014(2)	21.668(2)	21.874(3)	21.739(2)	22.265(2)	22.367(5)
b (Å)	12.2313(10)	12.3168(12)	12.2929(14)	12.3474(11)	12.4098(13)	12.499(3)
c (Å)	4.6081(4)	4.5234(4)	4.5796(5)	4.5384(4)	4.7070(5)	4.7060(10)
unit cell volume (Å^3)	1240.8(2)	1207.2(2)	1231.4(2)	1218.20(19)	1300.6(2)	1315.7(5)
ρ_{calcd} (g cm^{-3})	7.716	8.051	7.853	7.995	9.341	6.213
abs coeff (mm^{-1})	45.150	48.373	46.349	47.889	94.449	63.525
extinction coeff	0.00060(3)	0.00074(4)	0.00062(3)	0.00078(6)	0.00057(4)	0.00009(1)
GOF on F^2	1.067	1.277	1.095	1.046	1.098	1.078
data/params	1544/74	1498/74	1522/76	1515/76	1604/70	1618/70
R_1 ($I > 2\sigma_{(I)}$)*	0.0241	0.0243	0.0276	0.0311	0.0260	0.0231
wR_2 ($I > 2\sigma_{(I)}$)*	0.0525	0.0587	0.0565	0.0740	0.0680	0.0509
R_1 (all data)	0.0299	0.0280	0.0385	0.0395	0.0278	0.0275
wR_2 (all data)	0.0549	0.0599	0.0606	0.0781	0.0687	0.0520
largest peak/hole (e$^-$ Å^{-3})	2.76/−2.21	1.98/−1.75	2.09/−2.42	2.57/−1.86	2.40/−2.61	3.04/−2.27

*$R_1 = \sum||F_o| - |F_c||/\sum|F_o|$; $wR_2 = [\sum[w(F_o^2 - F_c^2)^2]/\sum[w(F_o^2)^2]]^{1/2}$, and $w = 1/[\sigma^2F_o^2 + (AP)^2 + BP]$, $P = (F_o^2 + 2F_c^2)/3$; A and B are weight coefficients.

Many reactions were set up with the goal to synthesize this compound; however, they yielded either $CaMn_2Sb_2$[27] or the new phase $Ca_8Mn_7Sb_6$.[38] As the listed unit-cell parameters suggest, its structure is related to the structure under consideration, but it is significantly more complex and not devoid of disorder (see the Supporting Information). The reactions aimed at the corresponding Sr-, Ba- and Eu-analogs also failed (using both stoichiometric and flux methods). The main products of these syntheses were Sr_2MnSb_2,[19] $SrMn_2Sb_2$,[27] Sr_2MnBi_2,[39] $BaMn_2Sb_2$,[29] $Ba_{32}Mn_{15}Bi_{32}$,[40] $EuMn_2Sb_2$,[41] and $Eu_{10}Mn_6Sb_{13}$.[21]

Powder X-ray Diffraction. X-ray powder diffraction patterns were taken at room temperature on a Rigaku MiniFlex powder diffractometer using Cu Kα radiation. The JADE 6.5 software package was used for the phase analysis. Powder patterns of the as-synthesized products from stoichiometric reactions revealed multicomponent mixtures with $A_{11}Pn_{10}$ and $A_{14}MnPn_{11}$ (A = Ca, Sr, Yb, Eu; Pn = Sb, Bi)[34] as the most common impurity phases. For flux reactions, portions of the isolated crystals were ground to powders and checked for uniformity; for experiments yielding crystals with different morphologies, they were segregated (whenever possible) on the basis of their physical appearance and ran separately. The intensities and the positions of the experimentally observed peaks and those calculated from the crystal structures matched very well. According to the powder diffraction patterns, the title compounds are stable in air for months.

Single-Crystal X-ray Diffraction. Crystals suitable for data collection were picked under a microscope in the glovebox, cut to the desired dimensions, and then mounted on glass fibers using Paratone N oil. The crystals of $Yb_9Mn_{4+x}Sb_9$, $Yb_9Zn_{4+x}Sb_9$ and $Yb_9(Mn,Zn)_{4+x}Sb_9$ were chosen from the corresponding Pb-flux or Pb/Zn-flux reactions, crystals of $Yb_9Mn_4Bi_9$ and $Ca_9Mn_4Bi_9$ had better quality from stoichiometric reactions. In all cases, multiple crystals were checked for singularity before selecting the best ones. Diffraction data (full spheres) were collected at 90 K on a Bruker SMART CCD-based diffractometer using monochromatized Mo Kα radiation. SMART software[42] was used to manage the data acquisition, done in batch runs at different ω and ϕ angles with frame width of 0.3−0.4° in ω and θ and exposure time of 10−20 s/frame. SAINTplus[43] was employed for the data integration and global unit-cell parameters refinements (all reflections). Semi-empirical absorption correction based on equivalents was applied using SADABS.[44] Initial atomic coordinates were taken from the structures of $A_9Zn_{4+x}Pn_9$ and $A_9Cd_{4+x}Pn_9$ (A=Ca, Sr, Yb, Eu; Pn = Sb, Bi; $0 \le x \le 0.5$),[25] and the subsequent refinement cycles (full matrix least-squares on F^2) were performed using SHELXL.[45] The extra electron density (ca. 12−14 e$^-$/Å^3, located approximately 2.6−2.7 Å away from Sb2 and Sb4) was modeled as Mn or Zn with fractional occupancy. Discernable residual peaks were present in the structures of all animonides, whereas the bismuthides appeared devoid of disorder. In all cases, site occupation factors were checked by freeing the site occupancy of an individual site, whereas the remaining parameters were kept fixed. Such trial refinements confirmed the mixing of Mn and Zn in the structures of the solid solutions $Yb_9Mn_{2.8}Zn_{1.6(1)}Sb_9$ and $Yb_9Mn_{0.5}Zn_{3.9(1)}Sb_9$. Detailed description of the latter refinements is provided as Supporting Information.

Selected data collection and structure refinements parameters for representative six crystals are given in Table 1. Atomic coordinates, equivalent isotropic displacement parameters for $Yb_9Mn_{4.18(2)}Sb_9$ and $Yb_9Mn_4Bi_9$ are presented in Table 2; important distances are listed in Table 3. Further information

(38) Xia, S.-Q.; Bobev, S. Unpublished results. $Ca_8Mn_7Sb_9$ is a new ternary phase, space group *Pnma*, a = 12.467(3) Å, b = 4.6227(9) Å, c = 44.067(8) Å. This structure is not fully established; preliminary structure refinements and a schematic drawing are provided in the Supporting Information.

(39) Saparov, B.; Bobev, S. Unpublished results. Sr_2MnBi_2 is isostructural and isoelectronic with Sr_2MnSb_2 (see ref 19). Crystal data: space group *Pnma*, a = 16.200(9) Å, b = 14.768(5) Å, c = 8.438(5) Å.

(40) Xia, S.-Q.; Bobev, S. Unpublished results. $Ba_{32}Mn_{15}Bi_{32}$ is a new ternary phase, space group *Imma*, a = 25.620(3) Å, b = 25.691(4) Å, c = 17.156(2) Å. This structure has extensive disorder and is not fully established; preliminary structure refinements and a schematic drawing are provided in the Supporting Information.

(41) Ruehl, R.; Jeitschko, W. *Mater. Res. Bull.* **1979**, *14*, 513–517.

(42) *SMART NT*, version 5.63; Bruker Analytical X-ray Systems, Inc.: Madison, WI, 2003.

(43) *SAINT NT*, version 6.45; Bruker Analytical X-ray Systems, Inc.: Madison, WI, 2003.

(44) *SADABS NT*, version 2.10; Bruker Analytical X-ray Systems, Inc.: Madison, WI, 2001.

(45) *SHELXTL*, version 6.12; Bruker Analytical X-ray Systems, Inc.: Madison, WI, 2001.

Table 2. Atomic Coordinates and Equivalent Isotropic Displacement Parameters (U_{eq}[a]) for $Yb_9Mn_{4+x}Sb_9$ ($x \approx 0.2$) and $Yb_9Mn_4Bi_9$

atom	Wyckoff	x	y	z	U_{eq} (Å)^2
		$Yb_9Mn_{4.18(2)}Sb_9$			
Yb1	2*b*	0	0	1/2	0.016(1)
Yb2	4*g*	0.13681(3)	0.13877(4)	0	0.015(1)
Yb3	4*g*	0.09172(2)	0.44414(4)	0	0.014(1)
Yb4	4*g*	0.26186(3)	0.38253(4)	0	0.016(1)
Yb5	4*h*	0.39790(3)	0.21899(5)	1/2	0.020(1)
Sb1	2*d*	0	1/2	1/2	0.013(1)
Sb2	4*g*	0.49792(4)	0.30629(7)	0	0.015(1)
Sb3	4*g*	0.30843(4)	0.12977(7)	0	0.016(1)
Sb4	4*h*	0.35132(4)	0.46537(6)	1/2	0.013(1)
Sb5	4*h*	0.16774(4)	0.31429(6)	1/2	0.013(1)
Mn1	4*h*	0.04483(9)	0.2821(2)	1/2	0.014(1)
Mn2	4*h*	0.24175(9)	0.1224(2)	1/2	0.014(1)
Mn3[b]	4*g*	0.3856(9)	0.363(2)	0	0.013(5)
		$Yb_9Mn_4Bi_9$			
Yb1	2*b*	0	0	1/2	0.020(1)
Yb2	4*g*	0.13809(3)	0.13676(5)	0	0.020(1)
Yb3	4*g*	0.09044(3)	0.43773(5)	0	0.019(1)
Yb4	4*g*	0.26494(3)	0.37891(5)	0	0.017(1)
Yb5	4*h*	0.39928(3)	0.21435(5)	1/2	0.020(1)
Bi1	2*d*	0	1/2	1/2	0.016(1)
Bi2	4*g*	0.49557(3)	0.30829(5)	0	0.017(1)
Bi3	4*g*	0.30995(3)	0.12493(4)	0	0.017(1)
Bi4	4*h*	0.35363(3)	0.46173(4)	1/2	0.016(1)
Bi5	4*h*	0.17080(3)	0.31542(4)	1/2	0.015(1)
Mn1	4*h*	0.0469(1)	0.2756(2)	1/2	0.021(1)
Mn2	4*h*	0.2425(1)	0.1138(2)	1/2	0.024(1)

[a] U_{eq} is defined as one-third of the trace of the orthogonalized U_{ij} tensor. [b] Refined as a partially occupied position. The final refined occupancy is 18(2)%.

in the form of crystallographic information files (CIF) have been deposited with Fachinformationszentrum Karlsruhe, 76344 Eggenstein-Leopoldshafen, Germany, (fax: (49) 7247−808−666; e-mail: crysdata@fiz.karlsruhe.de) − depository numbers CSD-420756 for $Yb_9Mn_{4.18(2)}Sb_9$; CSD-420757 for $Yb_9Zn_{4.18(2)}Sb_9$; CSD-420761 for $Yb_9Mn_{2.8}Zn_{1.6(1)}Sb_9$; CSD-420758 for $Yb_9Mn_{0.5}Zn_{3.9(1)}Sb_9$; CSD-420759 for $Yb_9Mn_4Bi_9$; and CSD-420760 for $Ca_9Mn_4Bi_9$. The combined CIF is provided as Supporting Information as well.

Magnetic Susceptibility Measurements. Field-cooled dc magnetization (M) measurements were performed using a Quantum Design MPMS2 SQUID magnetometer in the temperature interval 2−350 K and applied field of 1000 Oe (H). The measurements were done for different batches to ensure reproducibility. In all cases, polycrystalline samples were used, enclosed within gel-capsules. Several flux-grown $Yb_9Mn_{4.18(2)}Sb_9$ crystals were sufficiently large to afford measurements with the needles aligned both perpendicular and parallel to the direction of the applied magnetic field (needle direction presumed to be collinear with the shortest cell edge, i.e., the *c* axis). The raw magnetization data were corrected for the holder contribution and converted to molar susceptibility ($\chi_m = M/H$).

Resistivity Measurements. Four-probe resistivity measurements were carried out for a single crystal of $Yb_9Mn_{4.18(2)}Sb_9$ using a custom built system. Four Platinum wires (0.002 in.) were attached to the samples using EPO-TEK H_2O silver epoxy. A constant current of 1 mA was applied through the two outer leads and the voltages were measured between the inner two leads. At each temperature, the voltage was measured twice (with reversed current directions) in order to subtract any thermoelectric voltages formed at the junctions of dissimilar materials.

Table 3. Selected Interatomic Distances in $Yb_9Mn_{4+x}Sb_9$ ($x \approx 0.2$) and $Yb_9Mn_4Bi_9$

atom pair		distance (Å)	atom pair		distance (Å)
		$Yb_9Mn_{4.18(2)}Sb_9$			
Yb1−	4 × Sb2	3.3065(6)	Sb1−	2 × Mn1	2.844(2)
	2 × Sb4	3.3023(8)	Sb2−	2 × Mn1	2.747(1)
Yb2−	Sb2	3.132(1)		Mn3	2.57(2)
	Sb3	3.782(1)	Sb3−	2 × Mn2	2.734(1)
	2 × Sb4	3.1436(7)		Mn3	3.32(2)
	2 × Sb5	3.2232(7)	Sb4−	2 × Mn3	2.73(1)
Yb3−	2 × Sb1	3.1398(4)		Mn2	2.810(2)
	Sb2	3.696(1)	Sb5−	Mn1	2.736(2)
	Sb3	3.162(1)		Mn2	2.859(2)
	2 × Sb5	3.2619(7)	Mn1−	Sb1	2.844(2)
Yb4−	Sb3	3.259(1)		2 × Sb2	2.747(1)
	Sb3	3.399(1)		Sb5	2.736(2)
	2 × Sb4	3.1969(7)	Mn2−	2 × Sb3	2.734(1)
	2 × Sb5	3.2102(7)		Sb4	2.810(2)
Yb5−	Sb1	3.4987(6)		Sb5	2.859(2)
	2 × Sb2	3.3623(8)	Mn3−	Sb2	2.57(2)
	2 × Sb3	3.2227(8)		Sb3	3.32(2)
	Sb4	3.185(1)		2 × Sb4	2.73(1)
		$Yb_9Mn_4Bi_9$			
Yb1−	4 × Bi2	3.3480(5)	Bi1−	2 × Mn1	2.974(3)
	2 × Bi4	3.2933(7)	Bi2−	2 × Mn1	2.815(1)
Yb2−	Bi2	3.246(1)	Bi3−	2 × Mn2	2.796(2)
	Bi3	3.829(1)	Bi4−	Mn2	2.853(3)
	2 × Bi4	3.2080(6)	Bi5−	Mn1	2.803(3)
	2 × Bi5	3.3143(6)		Mn2	2.968(3)
Yb3−	2 × Bi1	3.1924(5)	Mn1−	Bi1	2.974(3)
	Bi2	3.7124(9)		2 × Bi2	2.815(1)
	Bi3	3.2118(9)		Bi5	2.803(3)
	2 × Bi5	3.3232(7)	Mn2−	2 × Bi3	2.796(2)
Yb4−	Bi3	3.3074(9)		Bi4	2.853(3)
	Bi3	3.4787(9)		Bi5	2.968(3)
	2 × Bi4	3.2396(6)			
	2 × Bi5	3.2485(6)			
Yb5−	Bi1	3.4792(7)			
	2 × Bi2	3.3904(7)			
	2 × Bi3	3.2750(7)			
	Bi4	3.2339(9)			

Computational Details. Electronic structure calculations were performed on $Yb_9Mn_{4+x}Sb_9$ using the linear muffin-tin orbital (LMTO) method[46] by the program "LMTO 4.7".[47] The Mn interstitial sites were not included. Exchange and correlation were treated in a local density approximation (LDA).[48] All relativistic effects except for spin−orbit coupling were taken into account by a scalar relativistic approximation.[49] Interstitial spheres had been inserted to achieve the space filling automatically.[50] The basis set included 5d, 6s, 6p for Yb; 3d, 4s, 4p for Mn; and 5s, 5p, 5d for Sb. The Yb 6p and Sb 5d orbitals were treated with the downfolding techniques.[51] The k-space integrations (512 k-points in the Brillouin zone) were performed by the tetrahedron method.[52] The energy at the Fermi level was selected as a reference.

(46) (a) Andersen, O. K. *Phys. Rev. B* **1975**, *12*, 3060–3083. (b) Andersen, O. K.; Jepsen, O. *Phys. Rev. Lett.* **1984**, *53*, 2571–2574. (c) Andersen, O. K.; Jepsen O.; Glötzel, D. In *Highlights of Condensed Matter Theory*; Bassani, F., Fumi, F., Tosi, M. P., Eds.; North Holland: New York, 1985. (d) Skriver, H. L. *The LMTO Method*; Springer: Berlin, 1984.
(47) Jepsen, O.; Andersen, O. K. The Stuttgart TB-LMTO Program, Version 4.7.
(48) Von Barth, U.; Hedin, L. *J. Phys. C* **1972**, *5*, 1629–1642.
(49) Koelling, D. D.; Harmon, B. N. *J. Phys. C* **1977**, *10*, 3107–3114.
(50) Jepsen, O.; Andersen, O. K. *Z. Phys. B* **1995**, *97*, 35–47.
(51) Lambrecht, W. R. L.; Andersen, O. K. *Phys. Rev. B* **1986**, *34*, 2439–2449.
(52) Blöchl, P. E.; Jepsen, O.; Andersen, O. K. *Phys. Rev. B.* **1994**, *49*, 16223–16233.

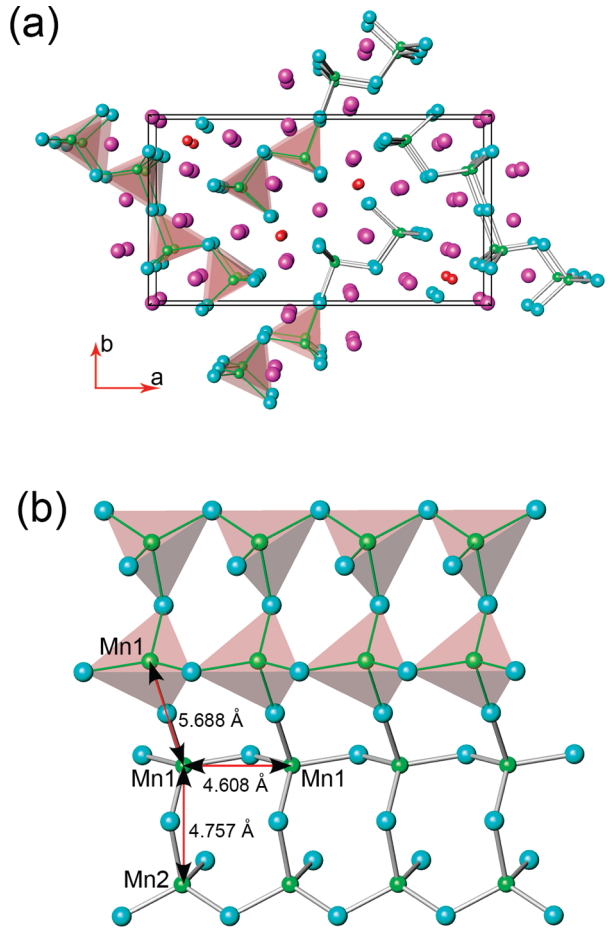

Figure 1. (a) Projection of the crystal structure of $Yb_9Mn_{4+x}Sb_9$ ($x \approx 0.2$), viewed down the *c*-axis. Unit cell is outlined. Bonds are drawn between the nearest Mn and Sb neighbors; the interstitial Mn sites are shown as isolated spheres. Yb, Mn, and Sb atoms were shown in purple, green, blue spheres, respectively; (b) polyhedral and ball-and-stick representation of the $[Mn_4Sb_9]$ chains. Selected Mn−Mn interactions are indicated.

In order to consider various Mn−Mn interactions for possible magnetic structures of $Yb_9Mn_4Sb_9$, a lower symmetry supercell was constructed by doubling the *c*-axis. Because this system contains 868 valence electrons for the $1 \times 1 \times 2$ supercell, it was necessary to treat the 4f-orbitals of Yb as core states when performing the spin-polarized calculations. A total of six different antiferromagnetic coupling schemes were chosen along the $^1_\infty[Mn_4Sb_9]$ chain direction, considering only the nearest-neighbor interactions (Figure 1).

The full potential linearized augmented plane wave method (FP-LAPW),[53] as implemented in the WIEN2k code[54] was used to gain better understanding of the magnetic order in the structure. In this method, the unit cell is divided into nonoverlapping muffin-tin (MT) spheres and an interstitial region. The wave functions in the interstitial regions are expanded in plane waves up to $R_{MT}K_{max} = 7$, where R_{MT} is the smallest radius of all MT spheres and K_{max} is the plane wave cutoff. The valence wave functions inside the MT spheres were expanded up to $l_{max} = 10$, while the charge density was Fourier expanded up to $G_{max} = 12$ (au)$^{-1}$. The MT radii were chosen to be 2.8 Bohr-units for the Yb atoms and 2.55 Bohr-units for the Mn and Sb atoms. The exchange correlation potential was calculated using the Perdew−Burke−Ernzerhof generalized gradient approximation (GGA).[55] Self-consistency was achieved using 2400 k-points in the irreducible Brillouin zone. The Brillouin zone integration was performed using the tetrahedron method, and the self-consistent calculations were considered to have converged if total energy and the charge of the system were stable within 1×10^{-4} *Ry* and 1×10^{-3} e^-, respectively.

Results and Discussion

Because a recent report has already discussed the subtleties of the bonding in the $A_9Zn_{4+x}Pn_9$ and $A_9Cd_{4+x}Pn_9$ (A = Ca, Sr, Yb, Eu; Pn = Sb, Bi; $0 \leq x \leq 0.5$) phases,[25] only a brief account, focused on the differences between the Mn and the Zn analogs, is provided herein. These considerations are illustrated in the following paragraphs by comparing the structures of $Yb_9Mn_{4+x}Sb_9$ and $Yb_9Zn_{4+x}Sb_9$, both with virtually identical percent filling of the interstitial positions.[56] The refined atomic coordinates, equivalent isotropic displacement parameters and selected interatomic distances for $Yb_9Mn_{4+x}Sb_9$ and for $Yb_9Mn_4Bi_9$ are given in Tables 2 and 3, respectively. The $Yb_9Mn_4Bi_9$ structure is briefly compared to that of $Ca_9Mn_4Bi_9$, but not discussed at length, as the bismuthides follow the same trends established for the antimonides. Further and more elaborate discussion can be found in previous reports for $Yb_9Zn_{4+x}Sb_9$ and $Yb_9Zn_4Bi_9$.[23,24]

Structure and Bonding. A structural representation of $Yb_9Mn_{4+x}Sb_9$ and $Yb_9Zn_{4+x}Sb_9$ ($x \approx 0.2$) is shown in Figure 1. The structure is orthorhombic, with space group *Pbam* (No. 55), and without the interstitial position is a direct analog of the $Ca_9Mn_4Bi_9$ type (Pearson's symbol *oP*44).[34] In a very simplistic description, the structure can be broken down to nine Yb^{2+} cations and Mn_4Sb_9 or Zn_4Sb_9 polyanionic sublattice of corner-shared $MnSb_4$ or $ZnSb_4$ tetrahedra. The latter are arranged into infinite chains running parallel to the *c*-axis, which are conjoined in an orthogonal direction to form tetrameric $^1_\infty[Mn_4Sb_9]$ and $^1_\infty[Zn_4Sb_9]$ units. There are no direct Sb−Sb interactions in the structure, and all Mn−Sb (Table 3) and Zn−Sb distances match very well with those reported for other tetrahedrally based arrangements, such as those in $Ca_{21}Mn_4Sb_{18}$,[17] Sr_2MnSb_2,[19] $CaMn_2Sb_2$,[27] $YbMn_2Sb_2$,[36] and $CaZn_2Sb_2$,[57] to name just a few. The corresponding angles deviate somewhat from the ideal tetrahedral value of 109.5°, ranging from 102.04(6) to 115.44(5)° in $Yb_9Mn_{4+x}Sb_9$, and from 101.17(5) to 117.30(4)° in $Yb_9Zn_{4+x}Sb_9$, respectively, but nothing out of the ordinary.

A particular point with regard to the distances and angles deserves a closer examination−the fact that the

(53) (a) Madsen, G. K. H.; Blaha, P.; Schwarz, K.; Sjöstedt, E.; Nordström, L. *Phys. Rev. B* **2001**, *64*, 195134. (b) Schwarz, K.; Blaha, P.; Madsen, G. K. H. *Comput. Phys. Commun.* **2002**, *147*, 71–76.

(54) Blaha, P.; Schwarz, K.; Madsen, G. K. H.; Kvasnicka, D.; Luitz, J. *WIEN2k, An Augmented Plane Wave + Local Orbitals Program for Calculating Crystal Properties*; Technische Universität Wien: Wien, Austria, 2001.

(55) Perdew, J. P.; Burke, S.; Ernzerhof, M. *Phys. Rev. Lett.* **1996**, *77*, 3865–3868.

(56) The structure of $Yb_9Zn_{4+x}Sb_9$ is known (see ref 24), but the percent filling of the interstitial position in the previous report was higher, making the direct comparison of the metrics difficult.

(57) Mewis, A. *Z. Naturforsch.* **1978**, *33B*, 382–384.

$MnSb_4$ tetrahedra in $Yb_9Mn_{4+x}Sb_9$ are less distorted than the $ZnSb_4$ tetrahedra in $Yb_9Zn_{4+x}Sb_9$. This is evidenced both from the angles mentioned above and from the distances, which show narrower distribution in $Yb_9Mn_{4+x}Sb_9$ compared to $Yb_9Zn_{4+x}Sb_9$. An inspection of the unit-cell metrics presented in Table 1 also points at some irregularities—the cell volume for $Yb_9Mn_{4+x}Sb_9$ is larger, as expected by comparing the sizes of Mn and Zn;[58] however, not all of the cell edges scale proportionally. The elongation of the *a*- and the *c*-axess on going from $Yb_9Zn_{4+x}Sb_9$ to $Yb_9Mn_{4+x}Sb_9$ is clear, 1.6 and 1.9%, respectively, whereas the *b*-axis is shortened by about 1% (Table 1). In terms of bonding, the net result is shorter Zn−Sb than Mn−Sb distances, with the exception of those in reference to Sb1 (Table 2). This Sb position (Wyckoff letter 2*d*) is the only one that does not have variable parameters and its coordination is strongly interrelated with the lattice parameters. Indeed, the Mn1−Sb1 distance (2.844(2) Å) is much shorter than the corresponding Zn1−Sb1 pair (2.950(2) Å). Similar in magnitude contraction of Mn1−Bi1 vs Zn1−Bi1 distances can also be inferred by comparing the *b*-axis of $Yb_9Mn_4Bi_9$ ($b = 12.4098(13)$ Å) and $Yb_9Zn_4Bi_9$ ($b = 12.5243(14)$ Å),[25] or $Ca_9Mn_4Bi_9$ ($b = 12.499(3)$ Å) and $Ca_9Zn_4Bi_9$ ($b = 12.5898(6)$ Å),[25] respectively. The same phenomenology pertains to the solid solutions $Yb_9Mn_{4+x}Sb_9$/$Yb_9Zn_{4+x}Sb_9$ (Table 1)—notice how the cell volume monotonically increases as the Mn content is increased from about 12 at % to about 64 at %, whereas the changes in the *b*-axis are opposite to this trend. Analysis of the other Mn−Sb, Mn−Bi, Zn−Sb, and Zn−Bi distances across the whole $Yb_9Mn_{4+x}Sb_9$ ($x \approx 0.2$), $A_9Mn_{4+x}Bi_9$ (A = Ca and Yb; $x \approx 0$) series reveals normal variations with the decreasing size of the transition metal. The dependence of the distances as a function of the phase width, as discussed in detail elsewhere,[25] is minimal.

Except for the partially occupied Mn or Zn sites, which explain the narrow homogeneity range, there are two crystallographically independent positions occupied by the d-metals in the structure. The mirror symmetry along the *c*-axis and the inversion symmetry at the Sb1 site will account for three unique Mn−Mn contacts. The longest Mn−Mn separation, which exists between the two Mn1 atoms connected to Sb1 is about 5.688(1) Å long. The other two Mn−Mn interactions are relatively stronger, as judged from the shorter distances: 4.6081(4) Å for Mn1−Mn1 along the direction of the *c*-axis, and 4.757(1) Å for Mn1−Mn2, respectively. These interactions are shown in Figure 1b. It should be pointed out here, that such Mn−Mn distances are much longer compared to those observed in related Mn-antimonides, such as $BaMn_2Sb_2$,[29] Sr_2MnSb_2,[19] $CaMn_2Sb_2$,[27] $Ca_{21}Mn_4Sb_{18}$,[17] $Sr_{21}Mn_4Sb_{18}$,[18] etc.

Properties. Reliable resisitivity measurements as a function of the temperature were possible only for $Yb_9Mn_{4+x}Sb_9$, for which sufficiently long and thick crystals could be synthesized. As the data shown in Figure 2 suggest, the sample is metallic in nature. The resistivity varies almost linearly with the temperature above 100 K, and shows a slight concave dependence at very low temperatures according to $\rho(T) = \rho_0 + AT^2$.[59] The value of the room-temperature resistivity is on the order of 2 mΩ cm, which together with the high residual resistance indicates poor metallic behavior. The value at 300 K is comparable to the resistivity of $Yb_9Zn_{4+x}Sb_9$ (ρ_{300} = 10 mΩ cm),[24] albeit slightly lower. This is somewhat unusual given that interactions of the "electron gas" with the spins are expected to decrease the conductivity, i.e., $Yb_9Mn_{4+x}Sb_9$ should be a poorer conductor than $Yb_9Zn_{4+x}Sb_9$. However, the higher resistivity of the latter could be an artifact of the lower density of states at the Fermi level in $Yb_9Zn_{4+x}Sb_9$ ($x \approx 0.4$), compared to $Yb_9Mn_{4+x}Sb_9$ ($x \approx 0.2$).

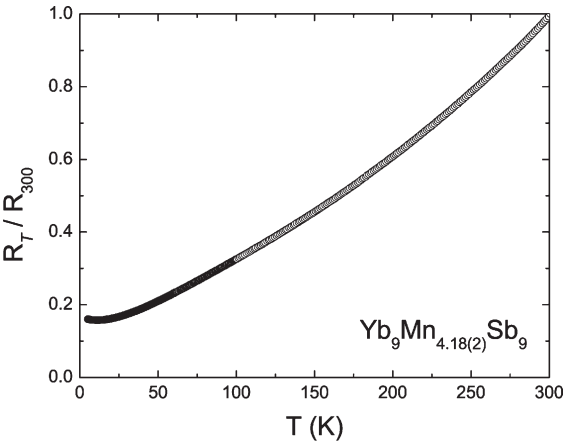

Figure 2. Four-probe electrical resistivity as a function of the temperature for a single-crystal of $Yb_9Mn_{4+x}Sb_9$ ($x \approx 0.2$). Data are normalized to the value at 300 K ($\rho_{300} \approx 2$ mΩ cm).

Plots of the temperature dependence of the magnetic susceptibility, $\chi = M/H$, of samples of $Yb_9Mn_{4+x}Sb_9$ ($x \approx 0.2$), $Yb_9Mn_4Bi_9$, and two different solid solutions $Yb_9(Mn,Zn)_{4+x}Sb_9$ are shown in Figure 3. The data for $Yb_9Mn_{4+x}Sb_9$ ($x \approx 0.2$) are gathered for single crystals; for the remaining three samples, only polycrystalline material was available. In analogy with $Ca_9Zn_4Bi_9$ and $Yb_9Zn_4Bi_9$, the behavior of $Ca_9Mn_4Bi_9$ is presumed to be similar to $Yb_9Mn_4Bi_9$, but the M vs T measurements were hampered because of small amounts of ferromagnetic $Ca_{14}MnBi_{11}$ impurity (with T_c of 55 K).[20]

The single-crystal dc magnetic susceptibility of $Yb_9Mn_{4+x}Sb_9$ measured with the applied field H parallel to the *c*-axis (the needle-direction) and for applied field parallel to the *ab* plane are quite similar (see the Supporting Information), and the former is plotted in Figure 3. The susceptibility gradually increases until about 100 K, where it shows a broad maximum (55−120 K), suggestive of short-range magnetic order. Above ca. 150 K, the magnetic behavior of $Yb_9Mn_{4+x}Sb_9$

(58) Taking the Shannon's ionic radii (see ref 37) of tetra-coordinate Mn^{2+} and Zn^{2+} as a reference point, 0.80 Å vs 0.74 Å, respectively.

(59) (a) Smart, J. S. *Effective Theories of Magnetism*; Saunders: Philadelphia, PA, 1966. (b) Kittel, C. *Introduction to Solid State Physics*, 7th ed.; John Wiley and Sons: Hoboken, NJ, 1996.

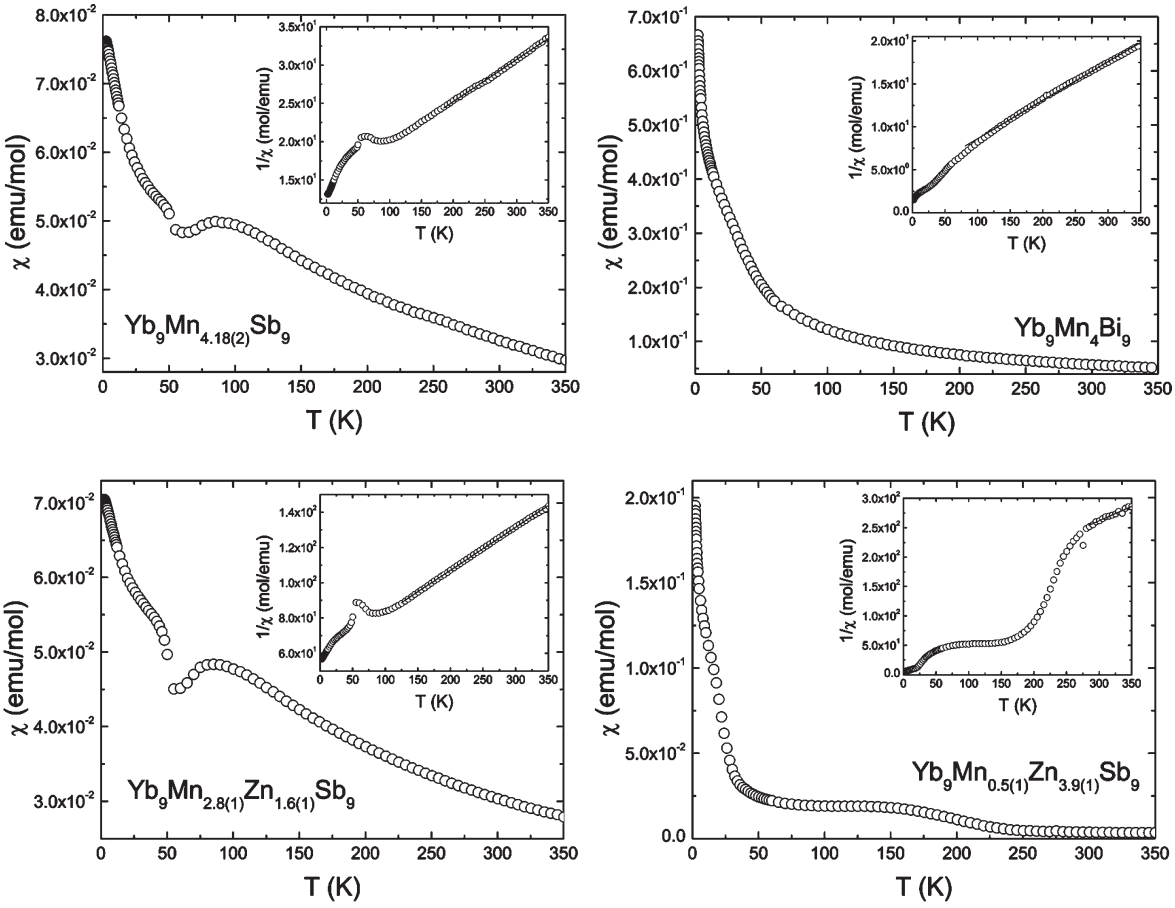

Figure 3. Temperature dependence of the magnetic susceptibility χ(T) for $Yb_9Mn_{4+x}Pn_9$ (Pn = Sb, Bi) and the solid solutions $Yb_9(Mn,Zn)_{4+x}Sb_9$ ($0 < x < 0.4$). The insets show the inverse magnetic susceptibility $\chi^{-1}(T)$ and the linear fits to the Curie−Weiss law (where applicable).

appears to be paramagnetic, which is evidenced by the plot of the inverse susceptibility vs the temperature, shown in the inset. As seen from the graph, $\chi^{-1}(T)$ follows the Curie−Weiss law $\chi(T) = C/(T - \theta_p)$, where $C = N_A\mu_{eff}^2/3k_B$ is the Curie constant and θ_p is the Weiss temperature. The calculated effective moment from the linear fit is about 12 μ_B/f.u., and the corresponding θ_p is −240 K. Because all previously measured Yb-compounds with this structure[25] had divalent Yb^{2+} ($\mu_{eff} = 0\,\mu_B$[59]), it is reasonable to expect the observed moment to be due solely to the Mn. Assuming that all Mn atoms contribute evenly to the susceptibility, the calculated moment is almost equal to the effective moment predicted by the Hund's rule for 4 Mn^{2+} ions ($3d^5$, $\mu_{eff} = 5.9\ \mu_B$[59]). The deeply negative θ_p value suggests strong antiferromagnetic coupling between the Mn spins, a hypothesis which is corroborated by the minimum at 50 K in $d(\chi T)/dT$. These facts could indicate the onset of long-range antiferromagnetic order.

The magnetic behavior of the Mn-rich $Yb_9Mn_{2.8}Zn_{1.6(1)}Sb_9$ is very similar to that of the undoped $Yb_9Mn_{4+x}Sb_9$, clearly showing the same characteristics (Figure 3). The calculated effective moment from the linear fit of $\chi^{-1}(T)$ is about 6.0 μ_B/f.u., and the corresponding θ_p is −220 K. The moment is 40% lower than what is expected for 2.8 Mn^{2+} ions, which can be a signature of increased counterbalancing coupling between Mn atoms on nonequivalent sites. In contrary, the calculated moment for the more "Mn-dilute" $Yb_9Mn_{0.5}Zn_{3.9(1)}Sb_9$ sample is 4.0 μ_B/f.u., a good match with the Hund's rule predictions. Here, one also encounters great difficulties with the rationalization of the temperature dependence of the susceptibility (Figure 3)—two very broad humps in $\chi(T)$, which can be attributed to either short-range magnetic order or reorientation of the Mn moments, and abrupt changes in $d(\chi T)/dT$ at ca. 210 K and ca. 20 K, suggestive of long-range magnetic order. It is also possible that small amount of unrecognized impurity (at levels below the detection limits of the X-ray powder diffraction, used to establish the sample quality) are present and interfere with the measurement. A similar explanation can be suggested for the last measured sample—$Yb_9Mn_4Bi_9$ (Figure 3). In this case, the slightly larger than expected calculated effective moment of about 13.2 μ_B/f.u. (θ_p is −130 K) and the sudden change of slope in $\chi^{-1}(T)$ at around 60 K are likely due to contribution of tiny amounts of $Yb_{14}MnBi_{11}$.[60]

All of the above brings us to the last point here−the agreement or the disagreement between the calculated and the expected spin-only moments. We argue that the experimental values should be taken with caution,

(60) Chan, J. Y.; Olmstead, M. M.; Kauzlarich, S. M.; Webb, D. J. *Chem. Mater.* **1998**, *10*, 3583–3588.

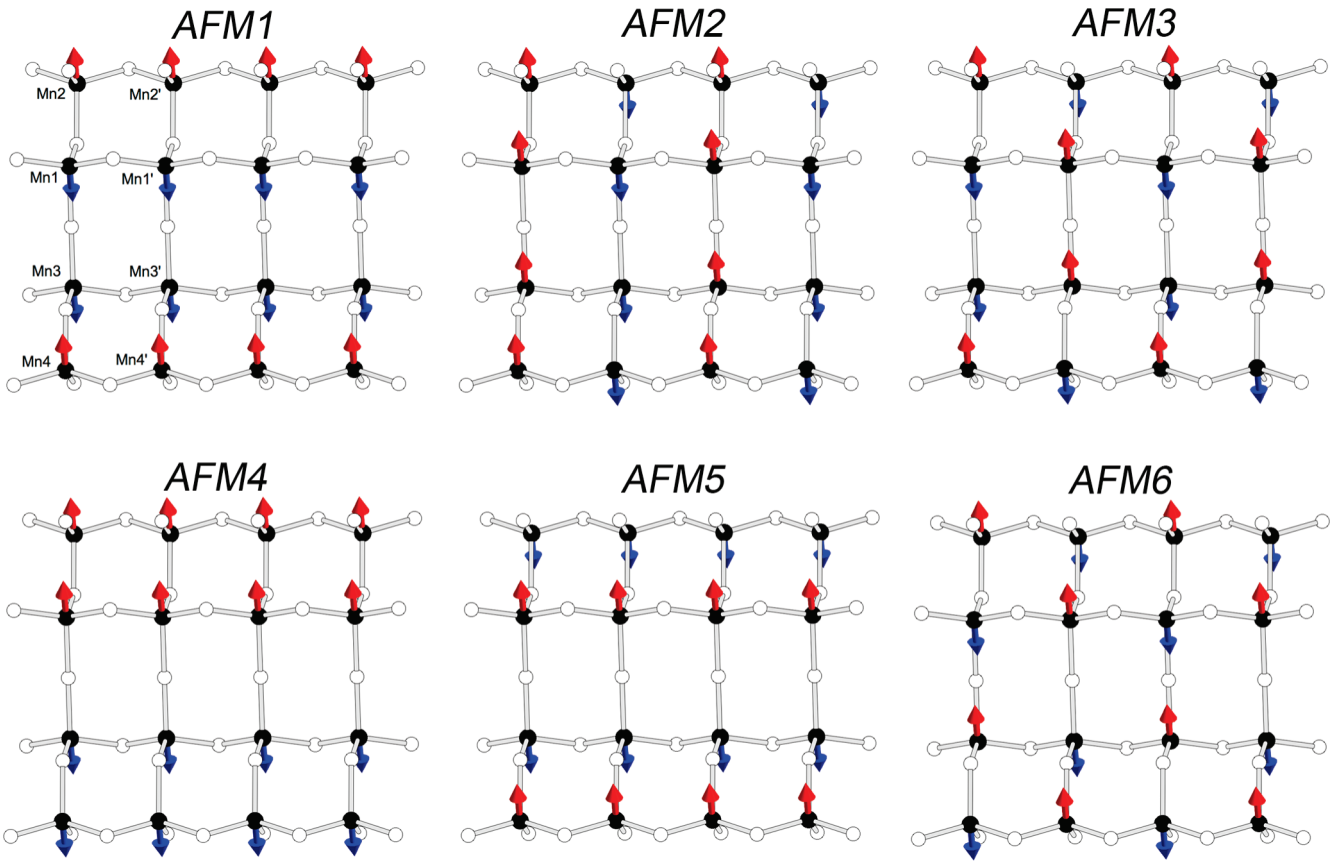

Figure 4. Schematic representations of six different models for antiferromagnetic coupling within the $[Mn_4Sb_9]$ anionic units. The models were constructed with the interstitial Mn sites removed and the *c*-axis doubled. Mn−Mn separations are indicated in Figure 1b; calculated moments are tabulated in Table 4. Mn1/Mn1′, Mn2/Mn2′, Mn3/Mn3′, and Mn4/Mn4′ are mirror images along $\bar{c}$ in the actual structure.

because prior experience shows that it is highly unlikely for a d-orbital magnetism in such condensed phases to be interpreted as if in a local-moment system.[26−29] Examples in the literature abound, particularly among the "14-1-11" phases,[61] where the electronic state of Mn had been erroneously assigned as Mn^{3+} ($3d^4$, μ_{eff}=4.9 μ_B[59]) in order to abide by the measured moments. In many cases, the origin of the magnetic interactions remains unclear even after neutron diffraction studies, underlying the difficulties in interpreting the magnetic behavior in such compounds.[62] Therefore, in the remaining part of this paper, we will turn our attention to theory, in an attempt to explain the magnetic interactions in this structure with $Yb_9Mn_{4+x}Sb_9$ as a lead example.

Electronic Structure. To fully understand the magnetizm in these new Mn-bearing antimonides, we carried out first-principle calculations using the local density approximation (LDA) with the aid of the Stuttgart LMTO program. A hypothetical 1 × 1 × 2 superstructure based on $Yb_9Mn_4Sb_9$ with the space group $Pmc2_1$ was built to configure six readily conceivable models with antiferromagnetically (AFM) coupled spins.[63] A schematic representation of these interactions and the naming of the Mn atoms is presented in Figure 4. It should be mentioned here that since such a supercell contains a very large number of atoms, the Yb 4f orbitals had to be treated as core states in order for the self-consistent iterations to converge. This simplification, although justified given the expected Yb^{2+} closed-shell configuration ($[Xe]4f^{14}$) could possibly miss some subtle magnetic contributions. Thus, we also performed the all-electron spin polarization calculations implemented in the program WIEN2k.[54]

Table 4. Local Magnetic Moments (μ_B) for the Mn atoms for Several Plausible AFM Models, Calculated Using the LMTO Code; Relative Total Energies (eV), with Respect to Total Energy of the Corresponding Non-Magenetic Ground State Are Also Shown[a]

model	Mn1/Mn1′	Mn2/Mn2′	Mn3/Mn3′	Mn4/Mn4′	ΔE_{TOT}
FM	4.14/4.18	4.24/4.24	4.17/4.13	4.23/4.23	−18.012
AFM1	4.06/4.11	−4.13/−4.13	4.11/4.06	−4.13/−4.13	−19.120
AFM2	3.96/−4.00	4.08/−4.08	3.99/−3.95	4.08/−4.08	−18.988
AFM3	3.93/−3.98	−4.07/4.07	3.97/−3.93	−4.07/4.07	−19.275
AFM4	4.05/4.10	4.17/4.16	−4.09/ −4.04	−4.15/−4.15	−19.040
AFM5	4.01/4.05	−4.11/−4.11	4.05/4.01	−4.10/−4.10	−19.632
AFM6	3.91/−3.95	−4.04/4.04	3.94/−3.90	−4.05/4.04	−19.602

[a] The atoms denoted with the prime-symbols are symmetry equivalent in the real structure (Table 2), but become independent in the model structure with a 2-fold super-cell. See text and Figure 4 for details.

(61) Holm, A. P.; Kauzlarich, S. M.; Morton, S. A.; Waddill, G. D.; Pickett, W. E.; Tobin, J. G. *J. Am. Chem. Soc.* **2002**, *124*, 9894–9898.
(62) Brock, S. L.; Greedan, J. E.; Kauzlarich, S. M. *J. Solid State Chem.* **1994**, *113*, 303–311.
(63) For the sake of simplicity, all calculations and comparisons of the total energy are carried out using a supercell with a doubled *c*-axis and reduced symmetry. This was done to treat crystallographically equivalent Mn sites as independent, although some magnetic structures—for example, models AFM1 and AFM5—could also be calculated using the actual cell parameters in appropriate space groups.

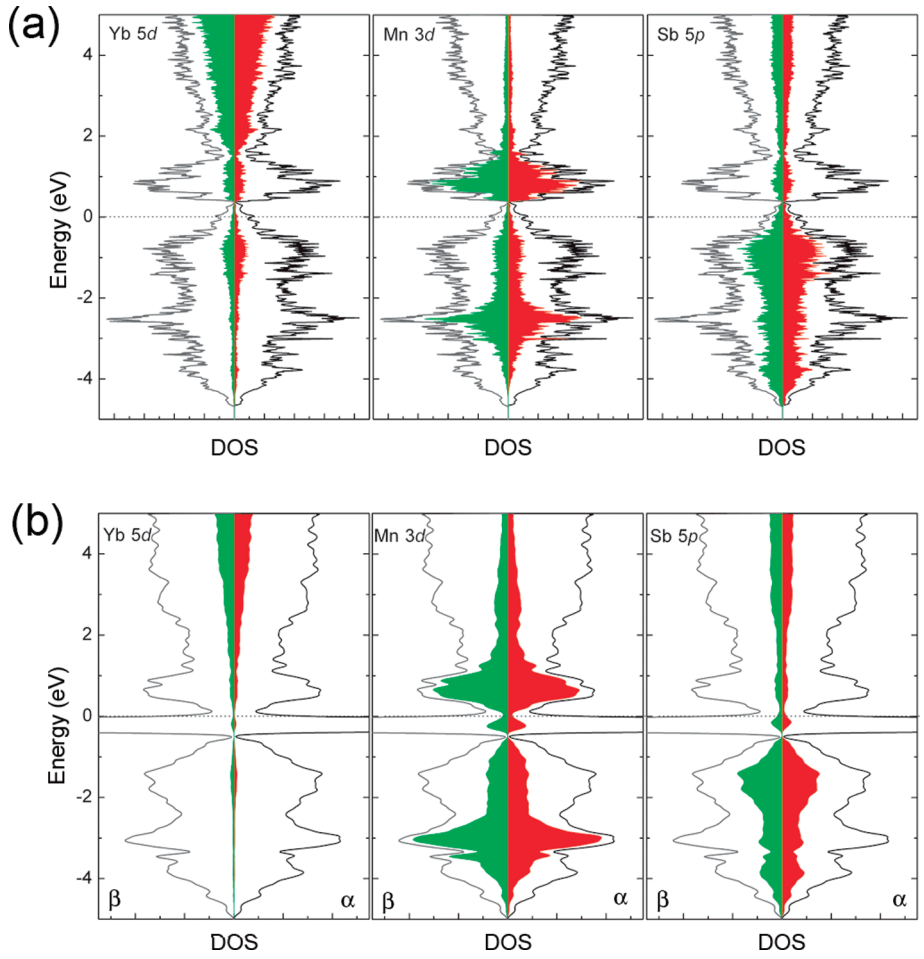

Figure 5. Calculated total DOS and partial DOS for the hypothetical 1 × 1 × 2 supercell. The results calculated by the (a) TB-LMTO-ASA and (b) FP-LAPW GGA methods are compared side by side. The right and left sides show the DOS for the majority (α) and minority (β) spins, respectively; the Fermi level has been set at zero energy (dashed line).

Relevant calculation results, including the total energies and the calculated magnetic moments on the different Mn sites, are provided in Table 4. From the tabulated data, it is clear that all AFM models are lower in energy compared to the FM structure, which supports the antiferromagnetic order inferred from the magnetization measurements (vide supra). Among the six models, the most stable one is AFM5 (Figure 5), which is about 100 meV/Mn lower in energy compared to the ferromagnetic (FM) arrangement. This energy difference is significant; however, it is much smaller than the 260 meV per Mn energy separation between the AFM and the FM structures of $CaMn_2Sb_2$, also calculated using the LDA approach.[27] These results indicate that the Mn−Mn antiferromagnetic coupling is weaker in $Yb_9Mn_4Sb_9$ than in $CaMn_2Sb_2$. Such conclusion is not surprising given that the Mn−Mn separation in the studied structure is larger than in $CaMn_2Sb_2$ (d_{Mn-Mn} = 3.178(2) Å).[27] In retrospect, the strength of the spin interactions could also be deduced from the much lower experimental magnetic moment in $CaMn_2Sb_2$ (0.2 μ_B/Mn) compared to 5.9 μ_B/Mn in $Yb_9Mn_{4.18(2)}Sb_9$.

The total DOS and selected partial DOS curves are plotted in Figure 5. Shown are the results obtained for model AFM5 by the LMTO code (excluding Yb 4f orbitals) and by the WIEN2k program (including Yb 4f orbitals). Both calculations suggest a pseudogap right above the Fermi level, indicating a slight electron deficiency for the hypothetical "empty" $Yb_9Mn_4Sb_9$ structure. This finding is consistent with our previous work on the interstitially stabilized $Sr_9Cd_{4.5}Sb_9$ (electron-precise phase), compared to the one-electron short $Sr_9Cd_4Sb_9$.[25] This analogy is helpful for understanding the electronic reason why extra Mn (up to 1/2 atom/f.u.) is found in tetrahedral voids of the $Yb_9Mn_{4+x}Sb_9$ structure—its polyanionic skeleton requires an additional electron but can tolerate small deviations from the optimal electron count. In parallel, a competition of the above-mentioned electronic factors and simple geometric considerations can be brought up as an explanation of the lack of interstitial atoms in both $A_9Zn_{4+x}Bi_9$ and $A_9Mn_{4+x}Bi_9$ (A = Ca and Yb; $x \approx 0$).

The DOS plots are also important for the following reasons: first, they confirm that for $Yb_9Mn_{4.18(2)}Sb_9$ and for any other $A_9Mn_{4+x}Sb_9$ or $A_9Mn_{4+x}Bi_9$ with "x" smaller than 0.5, the bonding should not be fully optimized, as the Fermi level cuts through a number of bands. Thereby, the metallic resistivity of $Yb_9Mn_{4.18(2)}Sb_9$ (Figure 2) can be understood. Second, the calculations show that despite the small electron deficiency, the Yb 4f

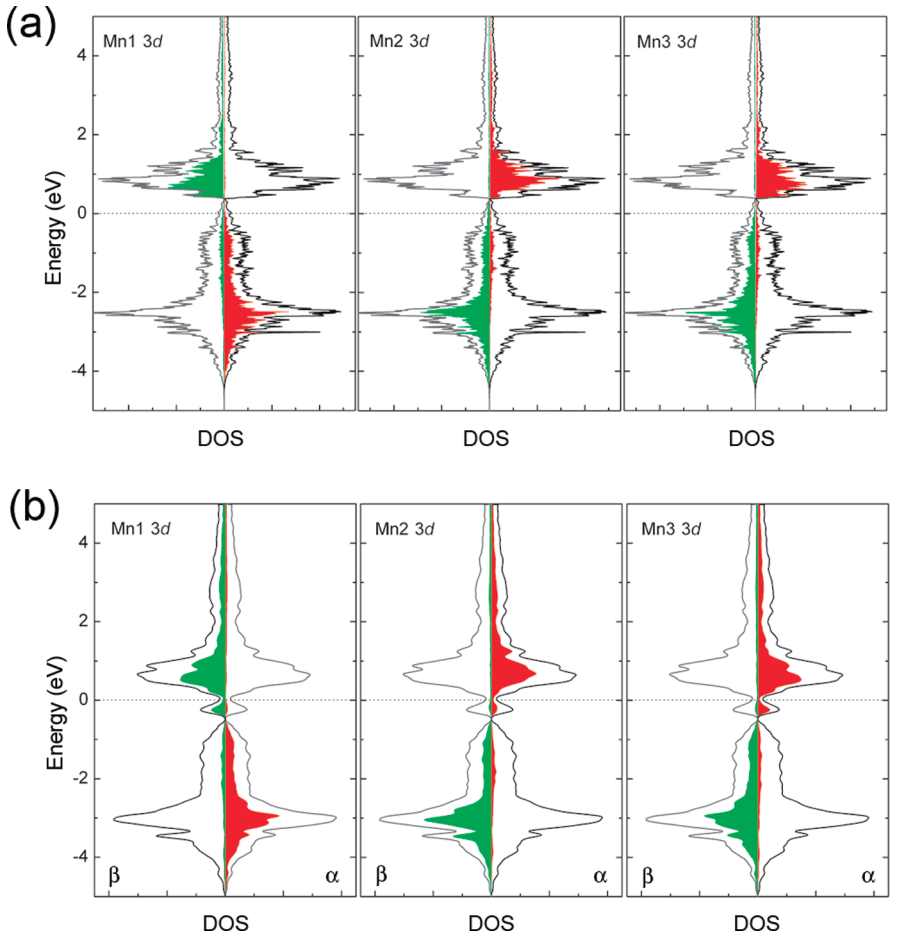

Figure 6. Projected DOS of 3d orbitals for different Mn atoms in the $Yb_{36}Mn_8Sb_{18}$ superstructure. The black curves represent the sum of all 3d states. (a) LMTO 4.7 calculation, and (b) WIEN2k calculations. The right and left sides show the DOS for the majority (α) and minority (*β*) spins, respectively; the Fermi level has been set at zero energy (dashed line).

states are basically localized and do not contribute to the overall electron count, corroborating the interpretation of the magnetic properties for the series of compounds (Figure 3). Third, both calculations (with or without the 4f states of Yb) support the antiferromagnetic ground state, which is also consistent with the magnetization measurements.

Within the context of this line of thoughts, it is worthwhile to briefly discuss the local magnetic moments of the Mn atoms. For this purpose, we refer to Figure 6, which presents the splitting of *M*n 3d orbitals obtained from the spin-polarized treatment. It is evident that the *M*n 3d states are separated into two parts—one is virtually filled and localized at relatively low energy (from 0 to −4 eV), whereas the other is basically empty in this region, but occupied right above the Fermi level. The latter states are contributing predominantly to the conduction bands. These characteristics support high spin (H.S.) configuration for the Mn atoms, in agreement with the proposed H.S. Mn^{2+} from earlier from neutron diffraction experiments.[36,62] GGA calculations resulted in very similar results, except that a small splitting appears right below the Fermi level, due to the existing of Yb 4f orbitals. However, the calculated moments are virtually identical, almost $4\,\mu_B$/Mn, coinciding with the LMTO calculations. These results further support the arguments that Yb should have negligible contribution to the magnetic properties, which originate only from interactions between the transition metal atoms.

Conclusions

The new ternary antimonide $Yb_9Mn_{4+x}Sb_9$ ($x \approx 0.2$) and the bismuthide $Yb_9Mn_{4+x}Bi_9$ ($x \approx 0$), as well as the solid solutions $Yb_9(Mn,Zn)_{4+x}Sb_9$ ($x < 0.4$) have been synthesized and structurally characterized by single-crystal X-ray diffraction. They crystallize with the orthorhombic space group *Pbam* and can be viewed as filled-variants of the $Ca_9Mn_4Bi_9$ type. All antimonide phases were found to exist in a narrow homogeneity range, while the bismuthides appear to be line compounds. Magnetic susceptibility measurements show that these materials have complex antiferromagnetically ordered structures. Spin-polarized LDA- and GGA-calculations provide further evidence for a structure, in which there is an antiferromagnetic coupling between the Mn spins and no contribution from the Yb atoms. Resistivity measurements indicate poor-metallic character, which is confirmed by the calculations as well.

The inherent nonstoichiometry in the whole $A_9M_{4+x}Pn_9$ series (A = Ca, Sr, Eu, Yb; M = Zn, Cd, Mn; Pn = Sb, Bi), and the ability of their structure to adapt to small variation in the electron count, make them

suitable candidates for transport property optimizations. In the light of the recent resurgence in studies on thermoelectric properties of some related phases,[2−10] this family of compounds might prove valuable for the identification of new high ZT materials. Based on the experimental results presented herein ($\rho_{300} \approx$ 2 m$\Omega \cdot$cm for $Yb_9Mn_{4+x}Sb_9$) and in earlier reports ($\rho_{300} \approx$ 10 mΩ cm for $Yb_9Zn_{4+x}Sb_9$), we believe that the electronic properties of the latter materials are on a par with the properties of $Yb_{14}MnSb_{11}$.[4] Preliminary thermopower measurements on unoptimized $Yb_9Mn_{4+x}Sb_9$ sample show S ≈ -20 μV/K at 300 K. Although only a crude estimate from a sample that might contain traces of Pb (from the flux), the value is also comparable with that of $Yb_{14}MnSb_{11}$.[4]

Given that this study also demonstrates the ability to form homogeneous solid solutions $Yb_9(Mn,Zn)_{4+x}Sb_9$, much like in $Yb_{14}Mn_xZn_{1-x}Sb_{11}$,[6] we speculate that by virtue of replacing Mn with Zn, spin-disorder scattering could be lowered, while maintaining optimal carrier concentration. Additionally, in analogy with the $Ca_{1-x}Yb_xZn_2Sb_2$ system,[8] it appears that the transport properties can also be altered through isoelectronic Yb−Ca substitutions. Both approaches show great promise for this system and call for further studies to accurately determine and tune the potentially useful properties of these materials.

Acknowledgment. S.B. acknowledges financial support from the University of Delaware and ACS-PRF (Award 47332-G10). S.-Q.X. thanks the Shandong University for the start-up grant.

Supporting Information Available: A combined X-ray crystallographic file in CIF format (all compounds). A plot of the single-crystal dc magnetic susceptibility of $Yb_9Mn_{4+x}Sb_9$ measured with the applied field H parallel to the *c*-axis (the needle-direction) and for applied field parallel to the ab plane, and crystal data and schematic representations of the tentative crystal structures of the new phases $Ca_8Mn_7Sb_6$ and $Ba_{32}Mn_{15}Bi_{32}$, which are not completely characterized yet (PDF). This material is available free of charge via the Internet at http://pubs.acs.org.